C−Cl Bond Rupture in Ultraviolet Photodissociation of Vinyl Chloride

Kenichi Tonokura,[†] Lizla B. Daniels,[‡] and Toshinori Suzuki*

Institute for Molecular Science, Myodaiji, Okazaki 444, Japan

Koichi Yamashita

Department of Chemical System Engineering, School of Engineering, The University of Tokyo, 7-3-1 Hongo, Bunkyo, Tokyo 113, Japan

Received: May 14, 1997; In Final Form: July 11, 1997[⊗]

Cl atomic elimination in ultraviolet photodissociation of vinyl chloride at 193 and 210 nm has been studied by photofragment ion imaging. The translational energy and angular distributions of the Cl fragments were measured for the two spin−orbit states of ^2P_J (J = 1/2, 3/2). The translational energy distributions of both of the ^2P_J fragments consist of two components; one is a Gaussian-like translational energy distribution with high anisotropy, $\beta = 1.0 \pm 0.2$, while the other is a statistical distribution with low anisotropy, $\beta = 0.3 \pm 0.2$. These features were almost identical for the two photoexcitation wavelengths. The anisotropy parameter, β, of the Gaussian translational energy component is in good agreement with the value predicted for the $\pi^* \leftarrow \pi$ transition by ab initio calculations. The high translational energy component of the Cl fragment is assigned to a prompt dissociation induced by the electronic relaxation from the (π,π^*) to (π(Cl),σ^*(C−Cl)) repulsive state, while the low translational energy component is assigned to a slow dissociation induced by the relaxation to the ground state. The [Cl*]/[Cl] fine structure branching has been found to be almost identical for the two dissociation pathways despite the large difference of the recoil velocities of the Cl atoms, suggesting an important role of the motion along the coordinate perpendicular to the C−Cl stretching in the nonadiabatic transition.

I. Introduction

Efficient intramolecular electronic and vibrational relaxation is an inherent property of polyatomic molecules and plays an essential role in their dynamics. The relaxation is often indicated by the variation of photophysical properties such as fluorescence quantum yield, emission wavelength, and lifetime of excited states; however, it may be manifested more clearly in photochemical reactions, since different relaxation pathways can lead to different products. The yield of these products, and the internal state, translational energy, and angular distributions provide detailed information about energy randomization and dissociation mechanisms.

A well-known example of electronic relaxation leading to photochemical reaction is an internal conversion from the (π,π^*) state to the ground state in ethylene that induces *cis*−*trans* photoisomerization. The potential energy surface (PES) of the (π,π^*) state of ethylene has a minimum at a perpendicular geometry of the two CH_2 groups, so that molecules undergo rapid C=C torsion upon photoexcitation.[1] At the perpendicular geometry, the (π,π^*) PES crosses with the ground state PES, which induces efficient *cis*−*trans* isomerization.[1] Since the internal energy thus gained is beyond the dissociation thresholds in the ground state, molecules undergo decomposition under collision-free conditions.[2] Halogenated ethylenes are interesting variations of ethylene, since their expected (π(X) or n(X),σ^*-(C−X); X = halogen) states lying below the (π,π^*) state induce branching of the electronic relaxation into the repulsive and the ground states.

Photodissociation of vinyl chloride (VCl) and dichloroethylenes (DCEs) have been studied by various experimental techniques,[3−9] and it has been established that electronic relaxation from the (π,π^*) state occurs to both the repulsive and the ground states in all of these systems. The former is manifested by the formation of Cl with fast speed and the latter by the formation of H, H_2, HCl, and slow Cl fragments. However, the branching of electronic relaxation upon 193 nm photoexcitation of DCE includes some complication due to the secondary dissociation,

$$DCE \rightarrow C_2H_2Cl + Cl(^2P_J) \quad \text{(primary)} \qquad \text{(i)}$$

$$C_2H_2Cl \rightarrow C_2H_2 + Cl(^2P_J) \quad \text{(secondary)} \qquad \text{(ii)}$$

Although this has not been examined in detail in earlier reports, recent work on 193 nm photodissociation of DCEs by photofragment translational spectroscopy (PTS) by Sato et al.[10] and our work on 235−193 nm photodissociation by photofragment ion imaging have shown that the fraction of secondary dissociation upon 193 nm photodissociation is considerably large. In the present work, the dynamics of C−Cl bond rupture in VCl is examined in detail, thus providing the basis to understand more complicated dissociation dynamics of DCEs.

The one-dimensional nonadiabatic transition and its role in fine structure branching in photodissociation of diatomic molecules have been extensively investigated theoretically[11,12] and experimentally.[12] However, the nonadiabatic transition in multidimensions has not been examined in detail. Since C−Cl bond rupture in photodissociation of VCl involves molecular deformation along various vibrational modes other than the C−Cl stretch, the fine structure branching in VCl involves

* Author to whom correspondence should be addressed. E-mail: suzuki@ims.ac.jp.

[†] Present address: Department of Chemical System Engineering School of Engineering, The University of Tokyo, 7-3-1 Hongo, Bunkyo, Tokyo 113, Japan.

[‡] JSPS Postdoctoral Fellow. Present address: Department of Geophysical Sciences, The University of Chicago, 5734 S. Ellis Ave., Chicago, IL 60637.

[⊗] Abstract published in *Advance ACS Abstracts,* September 1, 1997.

S1089-5639(97)01595-8 CCC: $14.00

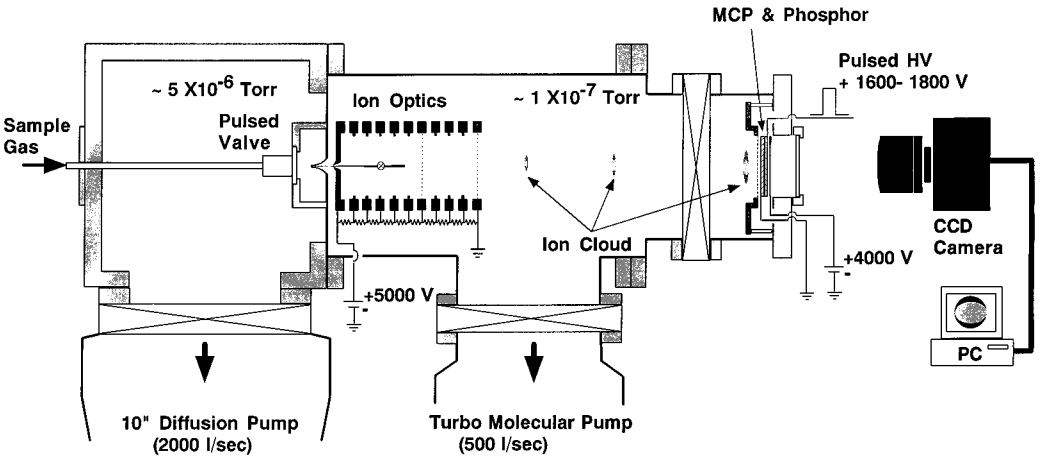

Figure 1. Schematic diagram of the experimental apparatus.

multidimensional dynamics. It is also noted that, if photodissociation of VCl undergoes two different dissociation channels, as reported previously,[5,7] it provides a unique opportunity for examining the fine structure branching for two different dissociation channels in the same molecule.

II. Experimental Section

(a) Apparatus. A schematic diagram of our experimental apparatus is shown in Figure 1. A sample gas seeded in He (0.2−7%) was expanded from a pulsed valve (General Valve Series 9, 0.8 mm orifice diameter) with a stagnation pressure of 700 Torr and collimated by two skimmers 0.5 mm in diameter. The molecular beam was introduced into a time-of-flight (TOF) mass spectrometer parallel to its electric field vector through the second skimmer embedded in the repeller plate. The beam diameter in the interaction region located 79 mm downstream from the nozzle has been measured to be 1 mm in the full width at half-maximum (fwhm). Typical pressures in the beam source and in the main chamber, with the pulsed valve on, were 5×10^{-6} and $\sim 1 \times 10^{-7}$ Torr, respectively. The rotational temperature of VCl molecules in the beam was estimated to be 10−30 K from the rotational analysis of $\tilde{A} \leftarrow \tilde{X}$ transitions of acetylene and NO measured under similar experimental conditions.

The molecular beam was perpendicular to the counterpropagated pump and probe laser beams. The output of an ArF excimer laser (Lambda Physik LPX110i) was used as a pump beam at 193 nm. The pump beam was polarized by a pile-of-plates polarizer with 10 quartz plates held at Brewster angle, for which a polarization degree of about 97% is expected. The pump beam at 210 nm was the second harmonic of the output of a Nd:YAG-pumped dye laser (Quanta-Ray GCR-230-25 and Lumonics HD-500). The second harmonic of the output of another dye laser (Quanta-Ray GCR-230-25 and Lumonics HD-500) was used as a probe beam at 235 nm. The [2+1] REMPI (resonance-enhanced multiphoton ionization) using the resonances of $4p\ ^2D_{3/2} \leftarrow 3p\ ^2P_{3/2}$ (235.336 nm) and $4p\ ^2P_{1/2} \leftarrow 3p\ ^2P_{1/2}$ (235.205 nm) was used for state-selective ionization of $Cl(^2P_J)$ atoms. The time delay between the pump and probe laser pulses was less than 20 ns. The pump beam was unfocused, while the probe beam was focused with an axisymmetric lens ($f = 250$ or 300 mm). The pump laser intensity was <1 mJ cm^{-2}/pulse at 193 nm and <2 mJ cm^{-2}/pulse at 210 nm. The probe laser intensity was reduced to <100 μJ/pulse to avoid a one-color signal. The intensities of the pump and probe laser beams were monitored by PIN photodiodes during the measurements.

The photoions produced were accelerated up to the kinetic energy of 5 keV and projected onto a dual microchannel plate backed by a phosphor screen (MCP; Hamamatsu, F2225-21PGFX, 36 mm in effective diameter). Although electric fields in the extraction and acceleration regions could be adjusted separately, the ion images were always measured with the same field strengths in the two regions to minimize an image distortion. A high-voltage pulse, 1600−1800 V in height and 200 ns in duration, was applied to the MCP to time-gate $^{35}Cl^+$ ions. The transient image on the phosphor screen was captured either by a video-rate CCD camera (Sony, XC77-CE) or by a Peltier-cooled CCD camera (Princeton Instruments, CCD-512SF). Images were typically integrated for 15 000−30 000 laser shots. During the integration of images, the probe laser frequencies were scanned over the entire Cl absorption line profiles that were broadened by the Doppler effect.

In order to examine any cluster formation in the molecular beam, images were measured for several VCl partial pressures from 0.2% to 7%. The features of the observed images, however, were invariant to the partial pressure, indicating that the effect of clustering on the observed signals was negligible. The sample purchased from Sumitomo Seika (purity > 99%) was used without further purification.

(b) Image Processing. An image experimentally observed is the two-dimensional (2D) projection of a cylindrically symmetric three-dimensional (3D) distribution of photofragment ions. A recoil velocity distribution (a differential cross section) is obtained from a section of the 3D distribution that is reconstructed from the 2D projection by an inverse Abel transform.[13] The transform inherently requires that the 2D projection is symmetric for the left and right sides of the symmetry axis, while an observed image often exhibits slight asymmetry due to nonuniform detection sensitivity of the apparatus. This slight asymmetry could not be avoided in the experiments, so that observed images were symmetrized by image processing prior to the transform. For symmetrization, two different image-processing procedures were employed in the present work. The first method was to average all of the four quadrants of an original image. The image generated by this method was symmetric for both of the left−right and upper−lower directions. The second method was to take only the left or right half of an image and synthesize a symmetric image by reflecting it to the other side. This method generated two images both of which were symmetric for the left−right but not for the upper−lower directions. The subsequent transform and analysis were performed independently on these two images. The purpose of the latter analysis was to estimate

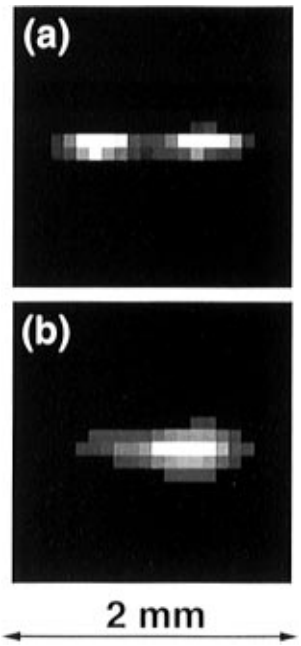

Figure 2. Images of NO^+ measured with a molecular beam of NO. The NO molecules were ionized by [2+1] REMPI via C state. Images a and b were measured under different focusing conditions of the probe laser beam.

the experimental uncertainty more critically than the former. It was found that the anisotropy parameters obtained by the second method starting from the left or right half of the original image were in agreement with each other within 10−20%. The values were also in good agreement with the one determined by the first method. The experimental uncertainty of angular anisotropy thus determined was estimated to be $\Delta\beta/\beta = 0.1-0.2$. This uncertainty is much larger than the standard deviation in each fitting of the angular distribution, and it should be taken as the largest bound. The experimental uncertainty in the determination of translational energy release, $P(E_T)$, is about 5% for all the translational energy range. Although we have not described in detail, the same procedure of the evaluation of an experimental uncertainty was used in our previous report on *trans*-DCE.[9] The uncertainty is similar between the present and previous works.[9]

The spatial resolution in ion imaging is limited by the ratio between the size of an image and that of a laser−molecular beams interaction region. In our experiments, the typical diameter of an image was 20 mm, while the effective laser−molecular beams interaction region was estimated to be less than 1 mm in length. The spatial resolution may be improved by deconvolution (deblurring);[14] however, such processing has not been performed in the present work. The difficulty of such deconvolution is that the point spread function (PSF), which is primarily the shape of the ionization region, cannot be determined accurately. As an example, an image of the molecular beam of NO (5% seeded in He) is shown in Figure 2. Since NO in the beam has negligible transverse velocity, the image primarily shows the shape of the laser−molecular beam interaction region. The probe laser beam (<100 μJ/pulse) was focused by an axisymmetric lens ($f = 250$ mm), and NO was ionized by [2+1] REMPI via the C state. The two images were measured under different focusing conditions of the probe laser beam. It is seen that the PSFs are different between the two conditions. Therefore, considering such a variable shape of PSF, resolution enhancement by debluring has not been attempted in the present study.

When the 2D data contain much noise, an inverse Abel transform collapses. In order to avoid such a collapse and make the numerical calculation stable, filtering of high-frequency components is sometimes employed. However, no filtering was performed in our study. The transform was successfully performed without any filtering.

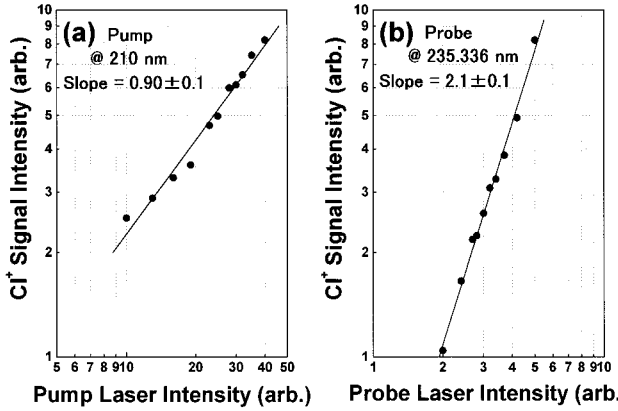

Figure 3. Laser power dependencies of the Cl REMPI signal. (a) Power dependence of the Cl^+ signal on the photolysis laser at 210 nm. (b) Power dependence on the probe laser at 235 nm.

(c) Power Dependence/Background Noise. In the measurements of Doppler profiles of Cl atoms and laser power dependence of the Cl^+ signal intensity, an output current of the MCP has been monitored, instead of an ion image. For this purpose, constant voltages were applied to both the MCP and phosphor screen, and the ac component in the phosphor voltage was monitored. The voltage between the back side of the MCP and the phosphor screen was set to 100 V. The ion signal was fed into a boxcar integrator (Stanford Research Systems, SR250) for averaging.

The typical dependence of Cl^+ signal versus pump laser power is shown in Figure 3a. The slope of 0.9 ± 0.1 suggests that it is a one-photon absorption process. Multiphoton excitation of the parent molecule and a secondary photodissociation of primary products by the pump laser are ruled out. On the other hand, a plot of the Cl^+ signal intensities versus the probe laser power shown in Figure 3b exhibits a slope of 2.1 ± 0.1. This is consistent with the [2+1] REMPI detection scheme of Cl atoms where the ionization step is saturated.

Although the observed Cl^+ signal depends upon pump and probe laser beam intensities as expected for the two-color signal, a small amount of background Cl^+ signals (<5%) was noticeable in ion images. The background Cl^+ signal appeared when the pump and probe laser beams are present, but it did not depend upon the probe laser frequency. An example of the background image is shown in Figure 4. The background ion images were subtracted from the data, prior to an inverse Abel transform.

III. Ab Initio Calculations

Ab initio calculations on the low-lying excited singlet states of VCl have been done by using the complete active space self consistent field (CASSCF) and internally contracted multireference configuration interaction (CMRCI) methods. The Gaussian basis set used in this work consisted of Dunning's correlation consistent polarized valence double- and triple-zeta basis sets, cc-pVDZ and cc-pVTZ.[15] For chlorine, these basis sets are extended by a set of s and p diffuse functions of even-tempered. This yielded a total of 140 contracted Gaussian functions for VCl (cc-pVTZ). The present calculations were carried out using the MOLPRO suite of ab initio programs.[16]

The experimental geometry of VCl[17] was used in the calculations. The ground state of VCl has the Hartree−Fock

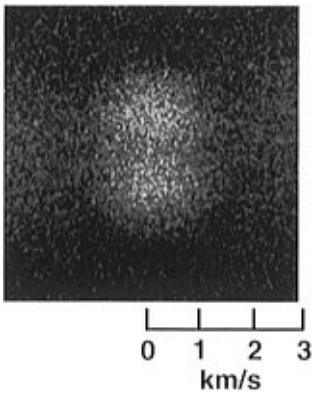

Figure 4. Image of the background Cl^+ signal which appeared with the photolysis and probe lasers but showed no dependence upon probe laser frequency. This two-color background signal was measured with the probe laser off-resonant with the Cl transition frequency.

configuration

$$(\text{core})(7a')^2...(11a')^2(12a')^2(2a'')^2(13a')^2(3a'')^2$$

For the CASSCF calculations, we have chosen eight electrons and six (12−14a′ and 2−4a″) orbitals as the active space, and three A′ and two A″ states were optimized in a state-averaged procedure with equal weights. The reference configuation state functions are 57 and 63 for the A′ and A″ symmetry, respectively. The CMRCI calculation, taking into account all the singly and doubly excited configurations from the CAS references, with the cc-pVTZ basis set resulted in 1.5×10^6 and 1.06×10^6 variational parameters (equivalent to 13 million in a conventional uncontracted MRCI), respectively, for the A′ and A″ symmetry. A higher order correlation correction was then included based on the formula of Feller and Davidson.[18] Table 1 summarizes the excitation energies and the transition dipole moments of five low-lying states.

IV. Results and Analysis

(a) Angular Distributions. The raw images of $Cl(^2P_{3/2})$ and $Cl^*(^2P_{1/2})$ atoms produced by 193 and 210 nm photodissociation of VCl are shown in Figure 5. The pump laser polarization (ϵ_{pump}) is vertical in all of the images. As an example, an inverse

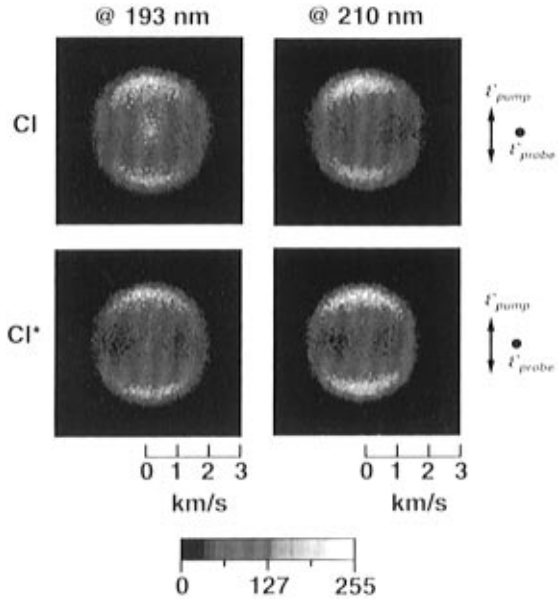

Figure 5. Raw (unsymmetrized) 2D images of $Cl(^2P_{3/2})$ and $Cl^*(^2P_{1/2})$ atoms produced by the photodissociation of vinyl chloride at 193 and 210 nm. The photodissociation laser polarization (ϵ_{pump}) is aligned vertically in the figure. The $Cl(^2P_{3/2})$ and $Cl^*(^2P_{1/2})$ atoms were detected by [2+1] REMPI of 4p $^2D_{3/2}$ ←— 3p $^2P_{3/2}$ at 235.336 nm and 4p $^2P_{1/2}$ ←— 3p $^2P_{1/2}$ at 235.205 nm, respectively.

Abel transform of the image in Figure 5a is shown in Figure 6a, which can be directly converted to a flux−velocity contour map of $Cl(^2P_{3/2})$ photofragments as shown in Figure 6b. From Figure 6, it is clear that the velocity distribution of Cl atoms consists of two components; one has a fast speed and high anisotropy, while the other has slow speed and low anisotropy. This feature is quite similar to that of Cl atoms produced by 235 nm photodissociation of *trans*-DCE reported previously.[9]

The angular distribution, $I(\theta)$, of photofragments can be calculated from the flux−velocity contour map. The angular distribution of photofragments is expressed by[19]

$$I(\theta) = (\sigma/4\pi)[1 + \beta P_2(\cos\theta)] \quad \text{(for a certain translational energy)} \quad (1)$$

where θ is the angle between the electric vector of the pump

TABLE 1: Calculated Excitation Energies (eV) and Transition Dipole Moments (au) for the Low-Lying Excited States of C_2H_3Cl

	CASSCF			CMRCI		
	cc-pVDZ	cc-pVTZ[a]	cc-pVTZ	cc-pVDZ	cc-pVTZ[a]	cc-pVTZ
			Total Energy (hartrees)			
1A′(gr.)	−536.995 231	−537.025 292	−537.030 268	−537.413 829	−537.498 882	−537.560 725
			Excitation Energy (eV)			
2A′(π^*←π)	8.630	8.421	8.405	7.642	7.381	7.399
3A′(σ^*←n)	9.012	8.873	8.897	8.676	8.484	8.490
1A″(σ^*←π)	7.717	7.596	7.638	7.363	7.223	7.262
2A″(π^*←n)	8.650	8.449	8.416	8.141	7.904	7.897
			Transition Dipole Moment (au)[b]			
⟨2A′|x|1A′⟩	0.5197	0.5506	0.5502	0.4498	0.4739	0.4747
⟨2A′|z|1A′⟩	1.1689	1.1931	1.1977	1.3404	1.3507	1.3598
θ (deg)	66.03	65.23	65.33	71.45	70.67	68.52
⟨3A′|x|1A′⟩-	−0.0340	−0.0429	−0.0430	0.0196	0.0185	0.0149
⟨3A′|z|1A′⟩	0.1929	0.1872	0.1862	0.0575	0.0618	0.0663
θ (deg)	80.0	77.09	77.00	71.20	73.36	77.33
⟨1A″|y|1A′⟩	0.1273	0.1410	0.1392	−0.0185	0.0120	0.0116
⟨2A″|y|1A′⟩	−0.0100	0.0076	0.0081	−0.0037	−0.0240	−0.0293
			Anisotropy Parameter			
2A′(π^*←π)	1.07	1.11	1.10	0.80	0.84	0.95

[a] Without d function on the hydrogen and f function on the carbon and chlorine atoms. [b] The *zx* molecular plane with *z* axis along the C═C bond.

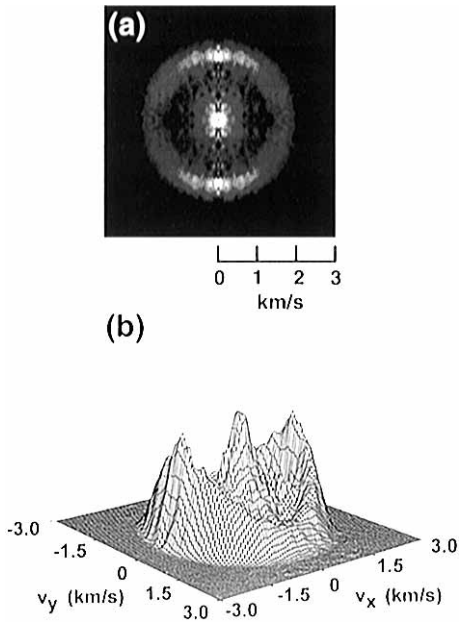

Figure 6. (a) Inverse Abel transform of the image shown in Figure 5a. (b) Surface plot of the flux−velocity contour map of $Cl(^2P_{3/2})$ atoms obtained from the image shown in part a.

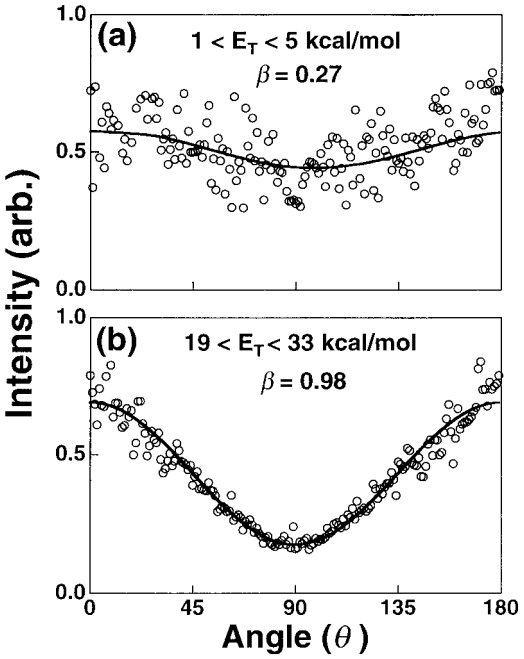

Figure 7. Angular distributions of $Cl(^2P_{3/2})$ atoms with the translational energy of (a) 1−5 kcal/mol and (b) 19−33 kcal/mol. The solid lines are the best fit of eq 1. Photodissociation wavelength was 193 nm.

laser and the recoil velocity, $P_2(x)$ is the second-order Legendre polynomial, and β is an anisotropy parameter, respectively. For an instantaneous dissociation, β is given by $2P_2(\cos\chi)$, where χ is the angle between the transition dipole moment (μ) in the parent molecule and the recoil velocity. The angular distributions for the low and high translational energy components were extracted from the 2D flux−velocity contour map and were analyzed separately using eq 1.

It is noted that the photofragment ion distribution generally depends upon two quantities,

$$\text{ion distribution} \propto I(\text{scat}) \times I(\text{det}) \qquad (2)$$

where I(scat) is the scattering distribution of neutral photofragments and I(det) is the ionization efficiency for photofragments. If I(det) varies with the scattering angle, the ion image cannot be directly used to discuss the photofragment angular distribution and detailed analysis on I(det) is required. The variation of I(det) occurs when there exists a correlation between recoil velocity, v, and angular momentum, J.[20] However, in the present case, the images of $Cl(^2P_J)$ ions were invariant to the probe laser polarization which is either parallel or perpendicular to the imaging plane, within an experimental error of 10%. Therefore, I(det) is considered to be constant over the scattering angle. Hereafter, we will consider a photoion distribution as a photofragment distribution, since these are identical in the absence of vector correlation.

Figure 7 presents the angular distributions of $Cl(^2P_{3/2})$ atoms with different translational energies produced by 193 nm photodissociation and the best-fit curves of eq 1. It is seen that the high- and low-energy components show largely different anisotropy parameters. The anisotropy parameters obtained are summarized in Table 2. Figure 8 shows the translational energy dependence of the anisotropy parameter, $\beta(E_T)$. The $\beta(E_T)$ increases to the high-energy side, primarily due to an increasing contribution of the high-energy anisotropic component.

(b) Translational Energy Distributions. The speed distributions, $P(v)$, of Cl photofragments were obtained by integrating the angular part of the flux−velocity maps. Then, transformation from the velocity to energy space was performed to obtain center-of-mass translational energy distributions, $P(E_T)$. The translational energy distribution is given by

$$P(E_T)\,dE_T = \frac{m_R}{m_{Cl}(m_{Cl}+m_R)}\frac{P(v)}{v}\,dv \qquad (3)$$

where m_{Cl} and m_R are the masses of a chlorine atom and a vinyl radical. The $P(E_T)$ for the Cl and Cl* channels in 193 and 210 nm photodissociation are shown in Figure 8. The features of the $P(E_T)$ were almost identical for the two different photoexcitation wavelengths, indicating that the dissociation mechanisms are essentially the same.

From the feature of $P(E_T)$, it is readily seen that the high-energy component can be approximated by a Gaussian function,

$$P(E_T)_{high} = A\exp[-\ln 2(E_T - E_{peak})^2/(\Delta E/2)^2] \qquad (4)$$

where A is a normalization constant, E_{peak} is the peak position, and ΔE is the width (fwhm) of the peak. The low-energy component is fitted by a statistical distribution function. We

TABLE 2: Anisotropy Parameters Determined for the Angular Distribution of Cl Atoms[a]

λ (nm)	$Cl(^2P_J)$ J	overall		β low E_T[c]	β high E_T[d]	ab initio	
		Umemoto[b]	this work			CASSCF, cc-pVDZ	CMRCI, cc-pVTZ
193	3/2	0.85	0.89(0.2)	0.26(0.2)	1.10(0.2)	1.07	0.95
193	1/2	0.85	0.94(0.2)	0.30(0.2)	1.09(0.2)		
210	3/2		0.85(0.2)	0.29(0.2)	1.00(0.2)		
210	1/2		0.85(0.2)	0.32(0.2)	0.96(0.2)		

[a] Estimated experimental uncertainties are indicated in parentheses. [b] The spin−orbit states are not resolved (ref 4). [c] The translational energy range of 1−5 kcal/mol. [d] The translational energy range of 19−33 kcal/mol.

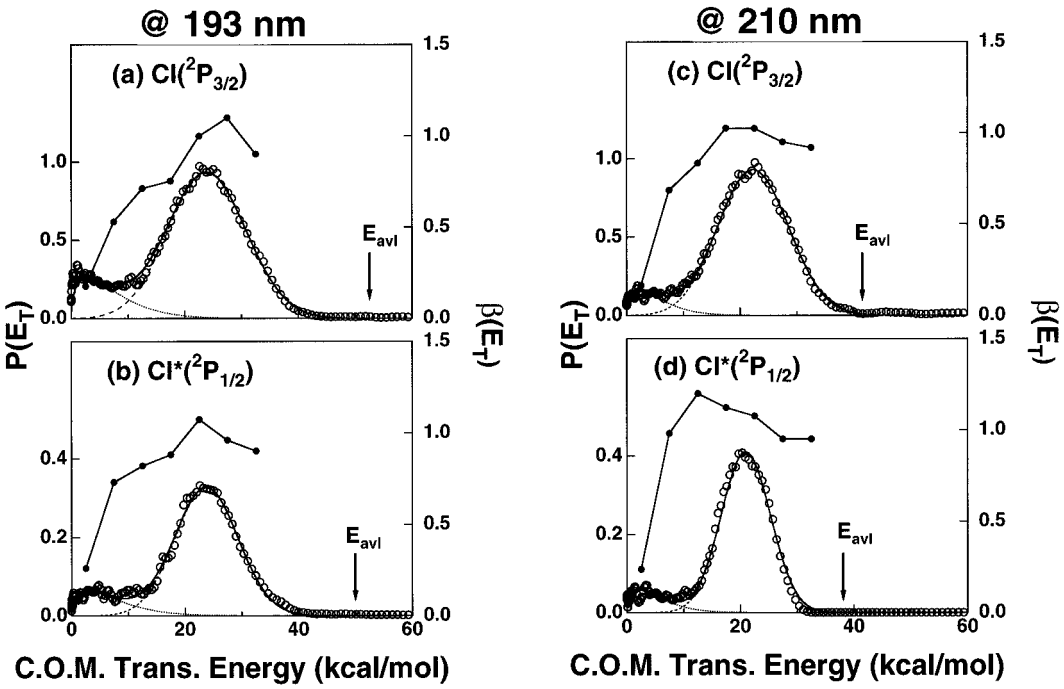

Figure 8. Center-of-mass translational energy release, $P(E_T)$ (○), and the anisotropy parameter, $\beta(E_T)$ (●), in the $Cl(^2P_J; J = 1/2, 3/2)$ atom elimination channel in 193 and 210 nm photodissociation of VCl. The dotted line (...) denotes the statistical distribution. The dashed line (- - -) denotes the Gaussian distribution. The solid line (—) denotes the sum of the two components. The parameters found for the functions are listed in Table 2. The available energies are marked by arrows.

TABLE 3: Center-of-Mass Translational Energy Release

	$Cl(^2P_J)$	overall	low E_T	high E_T		
λ (nm)	J	$\langle E_T \rangle$ (kcal/mol)	$\langle E_T \rangle$ (kcal/mol)	E_{peak} (kcal/mol)	fwhm (kcal/mol)	method
193		26				PTS, ref 4
193	3/2	23	1.6	25		MADS, ref 7
193	1/2	25				MADS, ref 7
193	3/2	22	6.81[a]	23.2[a]	16.5[a]	this work
193	1/2	23	6.5[a]	23.1[a]	13.0[a]	this work
210	3/2	22	5.2[a]	21.4[a]	14.1[a]	this work
210	1/2	19	4.9[a]	20.5[a]	9.8[a]	this work
193	3/2	22	4.4[b]	23.1[b]	16.4[b]	this work
193	1/2	23	5.6[b]	23.4[b]	13.1[b]	this work
210	3/2	22	4.5[b]	21.6[b]	14.9[b]	this work
210	1/2	19	4.7[b]	20.6[b]	10.4[b]	this work

[a] Analyzed using the prior distribution and Gaussian functions. [b] Analyzed using Maxwellian and Gaussian functions.

employed the prior distribution,[21]

$$P(E_T)_{low} = BE_T^{1/2}(E_{avl} - E_T)^{s+1/2}/E_{avl}^{s+2} \quad (5)$$

where B is a normalization constant, E_{avl} is the available energy, and s is the number of effective vibrational degrees of freedom in vinyl radical ($s = 3N - 6 = 9$), respectively.

The $P(E_T)$ values observed were analyzed by assuming a linear combination of eqs 4 and 5. The best-fit parameters obtained from each function are listed in Table 3, whereas the ratios of the yields of the low to high translational energy components are listed in Table 4. As seen in Table 3, the contribution of the low-energy component was found to be smaller than previous reports.[5,7b]

The low-energy statistical distribution can also be approximated by a Maxwellian, as has been performed in our previous paper on *trans*-DCE.[9] In fact, eq 5 transforms into a Maxwellian in the limit of $s \rightarrow \infty$,[22]

$$\lim_{s\to\infty} P(E_T) = B'E_T^{1/2} \exp(-E_T/kT) \quad (6)$$

The analysis assuming a Maxwellian function for the low-energy component was performed to examine any difference for different model functions. The best-fit Maxwellian distributions were characterized by the translational temperature $T = 1500-1900$ K or by the average translational energy $\langle E_T \rangle = 4-6$ kcal/mol. As shown in Table 3, the average translational energies thus obtained were in reasonable agreement with the values obtained with the prior distribution function.

TABLE 4: Ratio of the Low to High Translational Energy Components

	$Cl(^2P_J)$		
λ (nm)	J	$\Phi_{low E_T}/\Phi_{high E_T}$	method
193		0.24	PTS, ref 4
193	3/2	0.32	MADS, ref 7
193	1/2	0.12	MADS, ref 7
193	3/2	0.16	this work
193	1/2	0.15	this work
210	3/2	0.09	this work
210	1/2	0.10	this work

(c) Fine Structure Branching Ratio. The branching ratios into $Cl^*(^2P_{1/2})$ and $Cl(^2P_{3/2})$ were determined from the REMPI signal intensities. The signal intensities observed were corrected for the pump and probe laser intensities and the strengths of two-photon transitions, $^2P_{1/2} \leftarrow\leftarrow {}^2P_{1/2}$ and $^2D_{3/2} \leftarrow\leftarrow {}^2P_{3/2}$, to

TABLE 5: Fine Structure Branching Ratios [Cl*]/[Cl][a]

λ (nm)	overall	low E_T	high E_T	ref
193	0.30(0.05)			5
193	0.30(0.01)			6
193		0.14	0.35	7
193	0.27(0.03)	0.27	0.27	this work
210	0.32(0.03)	0.33	0.31	this work

[a] The numbers in parentheses are experimental errors (1σ).

TABLE 6: Fraction of the Each Component for Cl Photofragments

λ (nm)	Cl(^2P_J) J	low E_T	high E_T
193	3/2	0.11	0.68
193	1/2	0.03	0.18
210	3/2	0.06	0.70
210	1/2	0.02	0.22

obtain the population in each Cl(^2P_J) state. The relative strengths of these transitions were determined by comparing them to the $^2D_{3/2} \leftarrow\!\!\!-\!\!\!- {}^2P_{3/2}$ and $^2D_{3/2} \leftarrow\!\!\!-\!\!\!- {}^2P_{1/2}$ transitions for which the ratio $f(^2D_{3/2}\leftarrow\!\!\!-\!\!\!-{}^2P_{3/2})/f(^2D_{3/2}\leftarrow\!\!\!-\!\!\!-{}^2P_{1/2}) = 2.5$ has been reported.[23] The relative two-photon transition strength of $f(^2P_{1/2}\leftarrow\!\!\!-\!\!\!-{}^2P_{1/2})/f(^2D_{3/2}\leftarrow\!\!\!-\!\!\!-{}^2P_{3/2})$ was determined to be 0.9 ± 0.1, which is in good agreement with the values determined independently, 0.9 by Cao et al.[24] and 0.85 ± 0.1 by Liyanage et al.[25] The branching ratios thus determined are listed in Table 5. No significant difference is seen between the branching ratios in the high- and low-energy components, which will be discussed later.

Table 6 summarizes the overall branching in the Cl atomic elimination process. Both in 193 and 210 nm photodissociation, 70% of the products are formed in the $^2P_{3/2}$ state and in the high translational energy component.

V. Discussion

(a) Dissociation Pathways. In ultraviolet photodissociation of VCl, the following three Cl elimination processes need to be considered.

$$C_2H_3Cl + h\nu \rightarrow C_2H_3(\tilde{X}) + Cl \quad \text{(I)}$$

$$\rightarrow C_2H_3(\tilde{A}) + Cl \quad \text{(II)}$$

$$\rightarrow C_2H_2(\tilde{X}) + Cl + H \quad \text{(III)}$$

As we have shown above, the translational energy distribution observed consists of two components. Considering the available energies in these channels, the high-energy Gaussian component observed is unambiguously assigned to reaction I. On the other hand, all three reactions I−III need to be examined as the origin of the low-energy component.

Concerning reaction II, there has been no accurate measurement of the heat of formation of the $\tilde{A}$ state vinyl radical. However, recent ab initio calculations by Mebel et al. (MRCI+D-(7,7)/ANO(2+)** level)[26e] have predicted the heat of formation of vinyl radical in the $\tilde{A}$ state to be 128 kcal/mol, which provides the available energy for the formation of $C_2H_3(\tilde{A})$ in 193 nm photodissociation to be −1 kcal/mol (energetically forbidden) (Table 7). Although it is possible that the value turns into a slightly positive value in a higher level of calculations, this channel can be ruled out from its small available energy.

Since only the chlorine atoms are observed in the present study, if secondary C−H bond rupture occurs after the C−Cl rupture, reaction III is a subset of reaction I. On the other hand, if part of the C−Cl bond ruptures occur synchronously with C−H bond rupture or following it, they would appear differently from reaction I. The two-bond rupture process, however, seems unlikely in 210 nm photodissociation, since the available energy is only 8 kcal/mol for the Cl channel and 5 kcal/mol for the Cl* channel. We will discuss later a minor contribution of this channel in 193 nm photodissociation.

TABLE 7: Energetics of Cl Atom Elimination Processes at 0 K[a]

products	ΔH_f (kcal/mol)	E_{avl}^{193} (kcal/mol)	E_{avl}^{210nm} (kcal/mol)
$C_2H_3(\tilde{X}) + Cl$	95 ± 2	53	41
$C_2H_3(\tilde{A}) + Cl$	149	−1	
$HCCH + Cl + H$	128	19	7
$H_2CC + Cl + H$	177		

[a] Heats of formation listed in ref 26 were used. Available energies for the Cl*($^2P_{1/2}$) elimination are given by $E_{avl} - 2.5$ kcal/mol.

Thus, the major part of the low-energy component of Cl is due to reaction I via the ground state of VCl. In the following, this is further examined by the calculation of the reaction rate.

We have estimated the reaction rate $k(E)$ of the C−Cl bond rupture in the ground state using variational RRKM (Rice−Ramsperger−Kassel−Marcus) theory.[27] It was assumed that the $H_2C{=}CH$ moiety in the transition state geometry of $[H_2C{=}CH{-}Cl]^*$ has the same structure as the C_2H_3 radical. The potential along the C−Cl stretching (reaction) coordinate was modeled by a Morse potential function. Three vibrational modes, two C−Cl bending and one C=C torsion, were considered as translational modes. The reduction of the vibrational frequencies of the two bending modes was taken into account by the formula

$$\nu(r) = \nu(r_e) \exp[-\alpha(r - r_e)] \quad (7)$$

where r_e is an equilibrium C−Cl bond length, $\nu(r_e)$ is the vibrational frequency in the stable molecule. The α parameter in the expression of $\nu(r)$ was chosen to be 1.04/Å, which is an empirical value previously used by other workers.[28] The one-dimensional potential for C=C torsion used was

$$V_t(r,\theta) = (V(r)/2)(1 - \cos 2\theta) \quad (8)$$

where $V(r)$ was assumed to change gradually from the value for VCl to that for vinyl radical,

$$V(r) = V_0 \exp\{-a(r - r_e)\} + V_\infty[1 - \exp\{-a(r - r_e)\}] \quad (9)$$

V_0 was taken to be 60 kcal/mol, whereas V_∞ was 19.8 kcal/mol. The a parameter was chosen to be 1.5/Å.[29] Eight other vibrational modes were assumed to be *spectrator* modes which undergo only minor frequency change during the dissociation. The sum of states was calculated as a function of energy and C−Cl distance, and the transition state was defined at the position that provides the minimum of the sum of states. The vibrational frequencies used in the calculations are listed in Table 8. A direct count algorithm was used to calculate the sum of states of the spectator modes.[27a] The hindered rotor energy levels E_i and g_i were calculated from the harmonic oscillator or Pitzer rotor expression, depending on n_i, as previously described.[29] The rate constants thus calculated versus the excitation energy are shown in Figure 9. The dissociation rate was calculated to be on the order of 10^{11} s^{-1}.

In the dissociation from the ground state, there are other exit channels such as HCl, H, and H_2 eliminations. Therefore, the lifetime of a metastable ground state molecule is less than 10^{-11}

TABLE 8: Vibrational Frequencies Used in RRKM Calculations (cm^{-1})

reactant[a]	transition state[b]	mode
3125	3215	C−H stretching
3086	3156	C−H stretching
3037	3049	C−H stretching
1610	1411	C═C stretching
1374	1359	CH_2 deformation
1281	764	CH rocking
1036	1098	CH_2 rocking
724	r.c.[c]	C−Cl stretching
396	61[d]	C═C−Cl rocking
943	t.m.[e]	C═C twisting
897	944	CH_2 wagging
621	95[d]	CHCl wagging

[a] From ref 30a. [b] The vibrational frequencies of eight spectator modes were taken from ref 30b. [c] r.c. is a reaction coordinate. [d] The vibrational frequencies were variable with the critical configuration at each excitation energy. The values, 61 and 95 cm^{-1}, tabulated here are for 210 nm photoexcitation (E_{exc} = 136 kcal/mol). The transition state at this photoexcitation energy is located at the C−Cl bond distance of 3.7 Å. [e] Treated as a hindered rotation. All other modes were treated as harmonic oscillators.

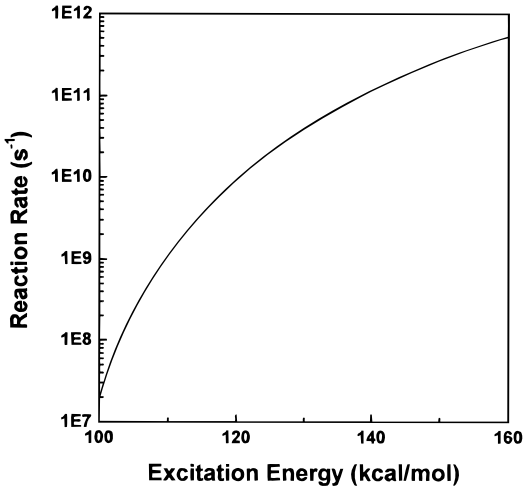

Figure 9. Rate constants calculated for the C−Cl dissociation in the ground state as a function of excitation energy.

s. Since the ratio of product yield [Cl]/[HCl] has been reported to be 1.1[4] and [Cl(via S_0)]/[Cl(via repulsive state)] ≈ 0.1, the lifetime of the metastable ground state molecule is expected to be in the picosecond range. This is in good agreement with the lifetime estimated from the anisotropy of the low-energy component as described below. Thus, the assignment of the low-energy component to the C−Cl rupture in the ground state is supported by this simple statistical calculation.

The nonbonding orbitals of Cl are classified as n(symmetric) or π(antisymmetric), depending on whether they are symmetric or antisymmetric for the reflection through the molecular plane. There are expected, therefore, two repulsive states of A′(n(Cl),σ*(C−Cl)) and A″(π(Cl),σ*(C−Cl)). Both of these states are expected to have a planar geometry at the minimum along the C═C twist coordinate, since the excitation does not affect the C═C bond. Umemoto et al.[4] have suggested that (1) the (n(Cl),σ*(C−Cl)) state is responsible for the rapid C−Cl bond rupture and that (2) the internal conversion to the ground state via the (π(Cl),σ*(C−Cl)) state is responsible for the slow bond rupture. However, since the (π,σ*) state is repulsive along the C−Cl coordinate, the latter does not seem the case.

The (π,σ*) state, in fact, is considered to be the pathway for the fast dissociation process. The observed kinetic energy release shows that a considerable amount of available energy is partitioned into internal excitation of vinyl radical in the high-energy dissociation component. If the (π,π*) state crosses a repulsive state in the Franck−Condon region, most of the available energy will be partitioned into the translational degree of freedom, just like a direct excitation to a repulsive state. Therefore, a crossing between the (π,π*) state and the repulsive state should be at much lower energy than the Franck−Condon region. The initial motion of the (π,π*) state is expected to be the C═C twist and C═C stretch by analogy with unsubstituted ethylene. The C═C twist plays a crucial role in the dynamics, since it breaks the plane of symmetry and induces the coupling between the A′(π,π*) and A″(π,σ*) states. Since the couplings of (π,π*) with both (n,σ*) and (π,σ*) states are allowed in twisted geometry, the assignment of the repulsive state responsible for the fast dissociation relies on an ab initio calculation of the excitation energies to these states. Although it has been predicted that the (π,σ*) state lies much lower than the (π,π*) state by ab initio calculations at the 4-31G level,[4] a higher level of ab initio calculations was necessary.

We performed ab initio calculations on the vertical excitation energy of the $\pi^* \leftarrow \pi$, $\sigma^* \leftarrow$ n, $\sigma^* \leftarrow \pi$, and $\pi^* \leftarrow$ n transitions in VCl with different levels of approximation from CASSCF/cc-pVDZ to CMRCI/cc-pVTZ (Table 1). From the comparison of the experimental (6.67 eV)[31] and theoretical values (7.38−8.63 eV) for the $\pi^* \leftarrow \pi$ vertical excitation energies, a scaling factor of 0.77−0.90 was deduced. Using this value and the vertical excitation energies predicted for the (π,σ*) and (n,σ*) states of 7.22−7.72 eV and 7.90−8.65 eV, the vertical excitation energies for these states are calculated to be 5.94−6.50 eV and 6.66−7.11 eV. Neither the 193 nm (6.4 eV) or 210 nm (5.9 eV) photoexcitation is sufficient in energy to reach the crossing point of the (π,π*) and (n,σ*) states. This suggests that the (π,σ*) state is responsible for the fast C−Cl bond rupture. Recently, Butler and co-workers[32] have reported that the (π,π*) state forms an avoided crossing with the (π,σ*) state at the C═C twisting angle degree between 20° and 30° by ab initio calculations (6-311G* level).

In our previous paper,[9] it was shown that anisotropy parameters determined for overall translational energy distributions are not adequate to discuss the dissociation mechanism. For example, in 193 nm photodissociation of *trans*-DCE, the anisotropy parameter determined for the overall translational distribution was 0.58 (Cl channel); however, this is an admixture of the contribution from the high-energy component (β = 1.25) and low-energy component (β = 0.26). The same is pointed out here for VCl. The angular anisotropy of the high-energy component is as high as 1.0, which indicates that VCl dissociates faster than its molecular rotation via this channel. Therefore, the anisotropy parameter may be compared with the value expected for an instantaneous dissociation. With an impulsive model, the β value observed leads to the angle (χ) between the transition dipole moment (μ) and direction of Cl recoil of 34 ± 2°. The expected value of β for an instantaneous dissociation from the ^{1}(π,π*) state was calculated from the transition dipole moment predicted by ab initio calculations. The calculated transition dipole moment was tilted by 23 ± 1° from the C═C bond toward the Cl atom in the ground state geometry, from which β is calculated to be 1.0 ± 0.1 for an instantaneous dissociation from the planar geometry. This is in excellent agreement with the experimental value. As seen in Table 1, from the magnitude of the transition dipole moment, the absorption cross section for the $\pi^* \leftarrow \pi$ transition much exceeds other transitions such as $\sigma^* \leftarrow$ n(Cl) and $\sigma^* \leftarrow \pi$(Cl); the photoabsorption cross section for the latter two are calculated

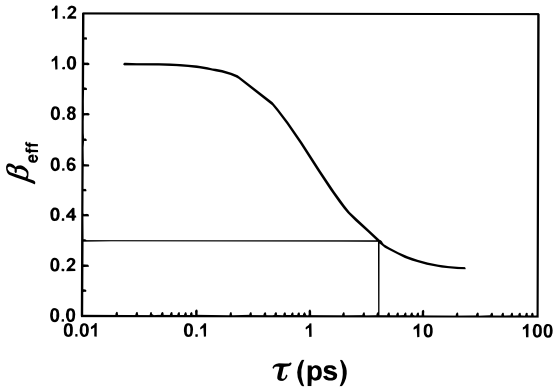

Figure 10. Reduction of the anisotropy parameter by the rotation of a photoexcited VCl molecule. The rotational temperature of VCl is assumed to be 20 K.

to be 40 times smaller than for the $\pi^* \leftarrow \pi$ transition. Thus, the contribution of direct excitation to the repulsive states is ruled out.

The peak position of the Gaussian component slightly changes (10%) with the increase of available energy (from 41 to 53 kcal/mol, $\Delta E/E = 20\%$). Since the excess energy on the (π,π^*) state is initially distributed to the C=C torsional and C=C stretching mode that are perpendicular to the C−Cl stretching coordinate, these energies will not be efficiently converted to repulsion energy along the C−Cl coordinate. Therefore, the translational energy of the fast Cl component is expected to be determined mostly by the position of the crossing between the (π,π^*) and (π,σ^*) states along the C−Cl stretching coordinate.

The reduction of the β value in the low energy component is ascribed to the loss of alignment by molecular rotation during the lifetime of photoexcited molecules. VCl is approximated by a prolate symmetric top with an asymmetry parameter, $\kappa = 0.98$. The dependence of an anisotropy parameter in the lifetime of the photoexcited molecule is calculated by[33]

$$\beta_{\text{eff}} = 2P_2(\cos\chi)\langle\langle D_{00}^{(2)}[\delta\Omega(t^*)]\rangle\rangle \tag{10}$$

where

$$\langle\langle D_{00}^{(2)}[\delta\Omega(t^*)]\rangle\rangle = (1/\tau^*)\int_0^\infty \exp(-t^*/\tau^*)\langle D_{00}^{(2)}[\delta\Omega(t^*)]\rangle \, \mathrm{d}t^* \tag{11}$$

Here the dissociation probability conforms to Poisson distribution with an average lifetime τ. The brackets denote a rotational correlation function which is evaluated from the expression[34]

$$\langle D_{00}^{(2)}[\delta\Omega(t^*)]\rangle = (b+1)^{1/2}(Y_{11} + Y_{12} + Y_{13}) \tag{12}$$

where the parameter b is given by $I_{\text{eff}}/I_Z - 1$,[35] and the Y_{ii} integrals are defined in Appendix B of ref 34. We have evaluated (11) and (12) numerically. The β_{eff} thus calculated versus lifetime, τ, is shown in Figure 10. Here $\tau^* = (kT/I_{\text{eff}})^{1/2}\tau$ has been calculated by assuming $T_{\text{rot}} = 20$ K.[36] From this figure, it is seen that β obtained for the low energy component, 0.3, corresponds to a lifetime of 4 ps, which is in reasonable agreement with the lifetime estimated from the variational RRKM calculations described above.

(b) Fine Structure Branching and Its Implications. It is noted that the ground state of VCl is adiabatically correlated to the $^2P_{3/2}$ state, but that the $^2P_{1/2}$ state is also produced in dissociation from the ground state. Note also that the recoil velocity is quite small in the dissociation from the ground state. In a one-dimensional nonadiabatic transition, adiabaticity can be expressed by the Massey adiabaticity parameter ξ,

$$\xi = \frac{R}{v}\frac{\Delta E_{\text{SO}}}{\hbar} \tag{13}$$

where R is the length of the interaction region of the potential curves, ΔE_{SO} is the energy separation of the interacting states, and v is the relative speed of separation. This one-dimensional model predicts that dissociation from the ground state produces predominantly Cl($^2P_{3/2}$). Therefore, the formation of the $^2P_{1/2}$ state from the ground state clearly indicates that the nonadiabatic transition is induced by the motion perpendicular to the C−Cl stretching coordinate, thus demonstrating the breakdown of the one-dimensional picture.

There is a small difference in the peak position and width of the Gaussian component between the two spin−orbit states of Cl(^2P_J) (Table 3). The difference of the width between the Cl and Cl* channels (∼4 kcal/mol) is larger than the spin−orbit splitting ($\Delta E = 2.5$ kcal/mol). The difference of the widths suggests that the nonadiabatic transition occurs at the C−Cl bond distance where the potential energy surfaces leading to Cl and Cl* still exhibit slightly different features along the coordinate perpendicular to the reaction coordinate. The [Cl*]/[Cl] branching ratio is lower than the statistical ratio, 0.5, suggesting that the excited state is more strongly coupled to the repulsive states leading to Cl than to those leading to Cl*.

In Figures 5 and 8, the contribution of the low-energy component is noticeably larger in the Cl than in the Cl* channel in the 193 nm photodissociation. The increase of Cl($^2P_{3/2}$) formation in dissociation at shorter photoexcitation wavelength has been observed more clearly in photodissociation of DCEs, which has been assigned to the opening of the secondary dissociation process:

$$C_2H_2Cl_2 \rightarrow C_2H_2Cl + Cl \quad \text{(primary)}$$

$$C_2H_2Cl \rightarrow C_2H_2 + Cl \quad \text{(secondary)}$$

In the secondary dissociation, the available energy is much smaller, so that an adiabatic dissociation to Cl($^2P_{3/2}$) will be more strongly favored than in the primary dissociation process, thus generating more low-energy Cl atoms. Thus, it is likely that the increase of the low-energy component of Cl in 193 nm photodissociation of VCl is due to the secondary dissociation as follows:

$$VCl \rightarrow C_2H_2Cl + H \rightarrow C_2H_2 + H + Cl$$

Our results is in agreement with the result of PTS of 193 nm photodissociation of VCl by Blank et al.[37]

The feature of the translational energy distribution of the Cl and Cl* elimination channels observed in the present study is similar to the one obtained by Umemoto et al.[4] using PTS. For further careful comparison, the overall distributions for (Cl + Cl*) were constructed from the $P(E_T)$ and the spin−orbit branching ratio determined in the present study (Figure 11). The shape of the $P(E_T)$ obtained in the present work shows a smaller distribution in the high-energy region (≥40 kcal/mol) than the one obtained by PTS. Since Umemoto et al.[4] employed an effusive beam, the high-energy tail previously observed is ascribed to the higher temperature of parent molecules.

As seen from Figure 8, the $P(E_T)$ for the Cl and Cl* channels in photodissociation of VCl were found to be almost the same in our experiment. The result is in disagreement with the previous report by Huang et al.[7] using MADS (magic angle Doppler spectroscopy), which showed significantly different $P(E_T)$ for the Cl and Cl* channels in 193 nm photodissociation of VCl. For direct comparison with the data reported by Huang

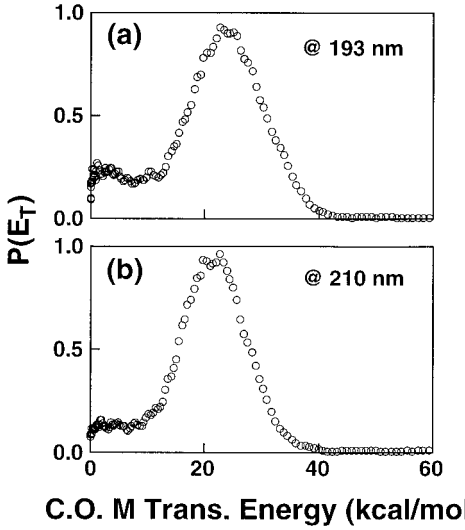

Figure 11. Overall translational energy distribution (Cl + Cl*) in photodissociation of VCl (a) at 193 nm and (b) at 210 nm. These distributions are generated from the $P(E_T)$ shown in Figure 8 and the fine structure branching ratio determined.

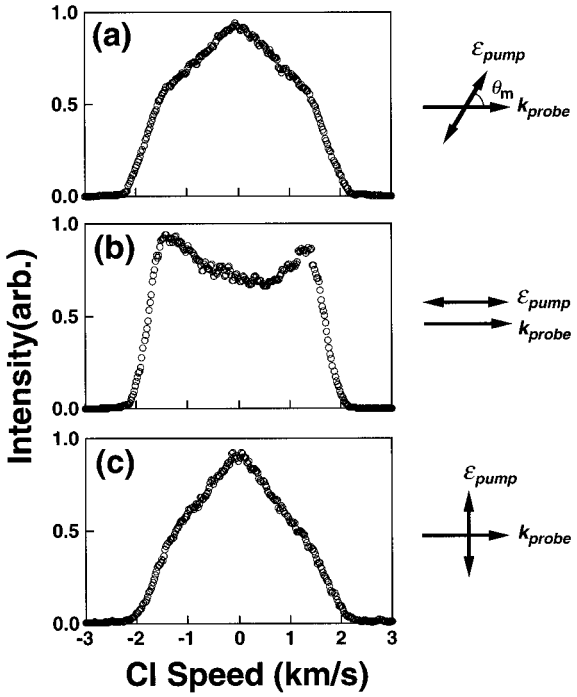

Figure 12. Line profiles expected for the magic angle and conventional one-dimensional Doppler spectroscopies. The profiles were constructed from the image in Figure 5a. (a) The polarization of the pump laser (ϵ_{pump}) is held at the magic angle (θ_m) with respect to the **k** vector of the probe laser (k_{probe}), (b) ϵ_{pump} is parallel to k_{probe}, and (c) ϵ_{pump} is perpendicular to k_{probe}.

et al. we have generated the Doppler line shape of $Cl(^2P_J)$ expected for MADS (Figure 12a), from the raw image shown in Figure 5. As seen in the figure, our data predict that shoulders will appear in the line shapes in MADS. Although the MADS profiles reported by Huang et al.[7] do not allow close inspection, there seems no indication of such shoulders in their spectra. The disagreement between the results obtained by 2D ion imaging and by MADS is even larger in the 193 nm photodissociation of *trans*-DCE.[7,9] It is pointed out, however, that the maximum energy releases determined by Huang et al. exceed the available energy calculated from the heat of formation, which suggests experimental ambiguity could be larger than their estimation.

The ratio of the Gaussian and statistical distributions determined in the present work is also smaller than the value reported by Mo et al.[5] using Doppler spectroscopy. For comparison, 1D Doppler profiles have also been generated from our raw image (Figure 12b,c). By comparing the generated profiles and those reported by Mo et al., the dip in the center of the line in (a) and shoulder in (b) are more pronounced in our simulation. It is pointed out again that the background signals shown in Figure 4 have been carefully subtracted from the data in the present work, which is considered to be one of the reasons for this difference.

In 1D Doppler spectroscopies that measure the 1D projection of the 3D velocity distribution, the speed distributions of photofragments are determined by least squares fitting of the experimental data with the assumed distribution functions. On the other hand, in a 2D experiment a well-established mathematical transform directly inverts the data into a speed−angular flux velocity contour map, which obviates any need for fitting or assumption. This difference should be emphasized in comparing these two methodologies. It is pointed out, however, that 1D "core-sampling" TOF spectroscopy provides better energy resolution than the 2D imaging method, so that the combination of these two methods is expected to be quite useful.

VI. Conclusion

The Cl elimination in the ultraviolet photodissociation of VCl has been studied by a state-resolved two-dimensional ion-imaging method. The velocity distribution of Cl and Cl* atoms consists of two components, a statistical translational energy distribution with low anisotropy and a Gaussian distribution with high anisotropy. Two components in the velocity distributions are attributed to the dissociation pathways via the repulsive and the ground states. Based on ab initio calculations, the repulsive state was assigned to the (π,σ^*) state. The fine structure branching ratio for the two dissociation pathways has been examined, and similar values have been found. Since the theory of a one-dimensional nonadiabatic transition predicts adiabatic dissociation into $C_2H_3 + Cl(^2P_{3/2})$ for the ground state channel, the result indicates an efficient nonadiabatic transition by the motion perpendicular to the C−Cl stretching coordinate. The slight increase of the low-energy Cl fragment in 193 nm photodissociation is attributed to the secondary dissociation of the C_2H_2Cl fragment. The fine structure branching is not statistical in both dissociation channels.

Acknowledgment. We thank H. Katayanagi for experimental assistance. This work was supported in part by a Grant-in-Aid from the Ministry of Education, Science, Sports and Culture (Nos. 07640694, 08559014, 09440208), Research Foundation for Opto-Science and Technology, and New Energy and Industrial Technology Development Organization.

Appendix

In a $Cl(^2P_J)$ atom, the coupling of orbital angular momentum L (=1) and electronic spin angular momentum S (=1/2) gives a total electronic angular momentum $J=L+S$ (=1/2, 3/2). Then, the coupling between J and nuclear spin angular momentum I (=3/2) gives rise to a composite angular momentum F, and J precesses about F. This hyperfine coupling depolarization is described by a time-dependent depolarization coefficient, $G^{(k)}(t)$.[38,39] The alignment parameter at time t, $A^{(k)}(t)$, is given by

$$A^{(k)}(t) = A^{(k)}(0)\, G^{(k)}(t) \qquad \text{(A1)}$$

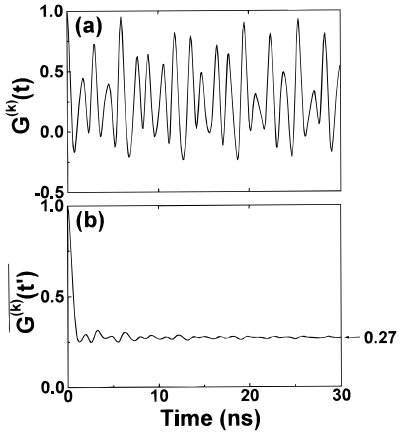

Figure 13. (a) Hyperfine depolarization coefficient for Cl atom for $J = 3/2$ and $k = 2$ calculated from eq A2. (b) Averaged hyperfine depolarization coefficient for Cl atom for $J = 3/2$ and $k = 2$ calculated from eq A3.

where $A^{(k)}(0)$ is an alignment parameter at time zero, and k is the order of alignment parameter, respectively. $G^{(k)}(t)$ is given by the following formula:[38,39]

$$G^{(k)}(t) = \sum_{F,F'} \frac{(2F'+1)(2F+1)}{2I+1} \begin{Bmatrix} F' & F & k \\ J & J & I \end{Bmatrix}^2 \cos[(E_{F'} - E_F)t/\hbar] \quad \text{(A2)}$$

where E_F is the energy of the F state.[40] The depolarization coefficient, $G^{(k)}(t)$, calculated for $J = 3/2$ and $k = 2$ versus time is shown in Figure 13a. It is seen that the $G^{(k)}(t)$ oscillates due to the procession of J about F. In the photodissociation experiments, since there exists time interval t' between dissociation and observation, the averaged depolarization coefficient, $\overline{G^{(k)}(t')}$, needs to be introduced:

$$\overline{G^{(k)}(t')} = \frac{1}{t'}\int_0^{t'} G^{(k)}(t)\, dt \quad \text{(A3)}$$

As seen in Figure 13b, the $\overline{G^{(k)}(t')}$ rapidly decays to the long time-averaged value, $G^{(k)}(t' \to \infty) = 0.27$. Under our experimental conditions, the pump and probe laser pulse duration of 6 ns and pump−probe time delay of <20 ns, the angular momentum polarization detectable is the time-averaged one. However, if $A^{(k)}(0)$ is reasonably large, it is still detectable. For example, in 355 nm photodissociation of Cl_2, alignment of $Cl(^2P_{3/2})$ fragments has been observed by REMPI-TOF technique using a transition of 4p $^2D_{3/2} \leftarrow\!\!\leftarrow$ 3p $^2P_{3/2}$.[41] Our result shows that there is no strong alignment of Cl atoms upon their formation in 193 and 210 nm photodissociation of VCl.

References and Notes

(1) (a) Buenker, R. J.; Bonaččić-Koutecký, V.; Pogliani, L. *J. Chem. Phys.* **1980**, *73*, 1836. (b) Ohmine, I. *J. Chem. Phys.* **1985**, *83*, 2348.

(2) Cromwell, E. F.; Stolow, A.; Vrakking, M. J. J.; Lee, Y. T. *J. Chem. Phys.* **1992**, *97*, 4029.

(3) Berry, M. J. *J. Chem. Phys.* **1974**, *61*, 3114.

(4) Umemoto, M.; Seki, K.; Shinohara, H.; Nagashima, U.; Nishi, N.; Kinoshita, M.; Shimada, R. *J. Chem. Phys.* **1985**, *83*, 1657.

(5) Mo, Y.; Tonokura, K.; Matsumi, Y.; Kawasaki, M.; Sato, T.; Arikawa, T.; Reilly, P. T. A.; Xie, Y.; Yang, Y.; Huang, Y.; Gordon, R. J. *J. Chem. Phys.* **1992**, *97*, 4815.

(6) (a) Reilly, P. T. A.; Xie, Y.; Gordon, R. J. *Chem. Phys. Lett.* **1991**, *178*, 511. (b) He, G.; Yang, Y.; Huang, Y.; Gordon, R. J. *J. Phys. Chem.* **1993**, *97*, 2186. (c) Huang, Y.; Yang, Y.; He, G.; Gordon, R. J. *J. Chem. Phys.* **1993**, *99*, 2752.

(7) (a) Huang, Y.; He, G.; Yang, Y.; Hashimoto, S.; Gordon, R. J. *Chem. Phys. Lett.* **1994**, *229*, 621. (b) Huang, Y.; He, G.; Yang, Y.; Hashimoto, S.; Gordon, R. J. *J. Chem. Phys.* **1995**, *103*, 5476.

(8) Sato, K.; Shihara, Y.; Tsunashima, S.; Umemoto, H.; Takayanagi, T.; Furukawa, K.; Ohono, S. *J. Chem. Phys.* **1993**, *99*, 1703.

(9) Suzuki, T.; Tonokura, K.; Bontuyan, L. S.; Hashimoto, N. *J. Phys. Chem.* **1994**, *98*, 13447.

(10) Sato, K.; Tunashima, S.; Takayanagi, T.; Fujisawa, G.; Yokoyama, A. Private communication.

(11) Singer, S. J.; Freed, K. F.; Band, Y. B. *Adv. Chem. Phys.* **1985**, *61*, 1.

(12) For example, the theoretical prediction by Alexander et al. (Alexander, M. H.; Pouilly, B.; Duhoo, T. *J. Chem. Phys.* **1993**, *99*, 1752) about photodissociation of HCl is in good agreement with the experimental results reported in ref 25.

(13) Abel transform code written by J. D. Myers at Pacific Northwest Laboratory.

(14) Strickland, R. N.; Chandler, D. W. *Appl. Opt.* **1991**, *30*, 1811.

(15) (a) Dunning, T. H. *J. Chem. Phys.* **1989**, *90*, 1007. (b) Kendall, R. A.; Dunning, T. H.; Harrison, R. J. *J. Chem. Phys.* **1992**, *96*, 6796. (c) Wood, D. E.; Dunning, T. H. *J. Chem. Phys.* **1993**, *98*, 1358.

(16) *MOLPRO* is a package of ab initio programs written by H.-J. Werner and P. J. Knowles with contribution from J. Almlöf, R. D. Amos, M. J. O. Deegan, S. T. Elbert, C. Hampel, W. Meyer, K. Peterson, R. Pitzer, A. J. Stone, and P. R. Tayor.

(17) Herzberg, G. *Molecular Spectra and Molecular Structure*; Van Nostrand Princeton: New York, 1967; Vol. III.

(18) Feller, D.; Davidson, E. R. *J. Chem. Phys.* **1984**, *80*, 1006.

(19) Zare, R. N. *Mol. Photochem.* **1972**, *4*, 1.

(20) Mo, Y.; Katayanagi, H.; Heaven, M. C.; Suzuki, T. *Phys. Rev. Lett.* **1996**, *77*, 830.

(21) Zamir, E.; Levine, R. D. *Chem. Phys.* **1980**, *52*, 253.

(22) Tsukiyama, K.; Bersohn, R. *J. Chem. Phys.* **1987**, *86*, 745.

(23) Tonokura, K.; Matsumi, Y.; Kawasaki, M.; Tasaki, S.; Bersohn, R. *J. Chem. Phys.* **1992**, *97*, 8210.

(24) Cao, J.; Loock, H.-P.; Qian, C. X. W. *Can. J. Chem.* **1994**, *72*, 758.

(25) Liyanage, R.; Yang, Y.; Hashimoto, S.; Gordon, R. J.; Field, R. W. *J. Chem. Phys.* **1995**, *103*, 6811.

(26) (a) Benson, S. W. *Thermochemical Kinetics*; Wiley Interscience: New York, 1976. (b) Ervin, K. M.; Gronert, S.; Barlow, S. E.; Gilles, M. K.; Harrison, A. G.; Bierbaum, V. M.; Depuy, C. H.; Lineberger, W. C.; Ellison, G. B. *J. Am. Chem. Soc.* **1990**, *112*, 5750. (c) Riehl, J.-F.; Morokuma, K. *J. Chem. Phys.* **1994**, *100*, 8976. (d) Riehl, J.-F.; Musaev, D. G.; Morokuma, K. *J. Chem. Phys.* **1994**, *101*, 5942. (e) Mebel, A. M.; Chen, Y.-T.; Lin, S.-H. Private communication. (f) Glukhovtsev, M. N.; Bach, R. D. *J. Phys. Chem. A* **1997**, *101*, 3574.

(27) (a) Halbrook, K. A.; Pilling, M. J.; Robertson, S. H. *Unimolecular Reactions*, 2nd ed.; Wiley Interscience: New York, 1996. (b) Forst, W. *Theory of Unimolecular Reactions*; Academic Press: New York, 1973.

(28) Sudbø, A. S.; Schulz, P. A.; Grant, E. R.; Shen, Y. R.; Lee, Y. T. *J. Chem. Phys.* **1979**, *70*, 921.

(29) Chesnavich, W. J. *J. Chem. Phys.* **1986**, *84*, 2615.

(30) (a) El-Sabban, M. Z.; Zwolinski, B. J. *J. Mol. Spectrosc.* **1968**, *27*, 1. (b) Wang, J.-H.; Chang, H.-C.; Chen, Y.-T. *Chem. Phys.* **1996**, *206*, 43.

(31) Robin, M. B. *Higher Excited States of Polyatomic Molecules*; Academic Press: New York, 1975; Vol. II.

(32) (a) Myers, T. L.; Kitchen, D. C.; Hu, B.; Butler, L. J. *J. Chem. Phys.* **1996**, *104*, 5446. (b) Browning, P. W.; Kitchen, D. C.; Arendt, M. F.; Butler, L. J. *J. Phys. Chem.* **1996**, *100*, 7765.

(33) Yang, S.-C.; Bersohn, R. *J. Chem. Phys.* **1974**, *61*, 4400.

(34) St. Pierre, A. G.; Steele, W. A. *Phys. Rev.* **1969**, *184*, 172.

(35) I_{eff} is the effective moment of inertia and I_Z is the moment of inertia around the symmetry axis of the symmetric top.

(36) The rotational time period is calculated to be 2.3 ps at 20 K.

(37) Blank, D.; Weizhong, S.; Suits, A.; Lee, Y. T.; North, S. W.; Hall, G. E. Unpublished.

(38) Zare, R. N. *Angular Momentum*; Wiley Interscience: New York, 1988.

(39) Blum, K. *Density Matrix Theory and Applications*; Plenum: New York, 1981.

(40) (a) Davis, L., Jr.; Feld, B. T.; Zabel, C. W.; Zacharias, J. R. *Phys. Rev.* **1949**, *76*, 1076. (b) Jaccarino, V.; King, J. G. *Phys. Rev. A* **1951**, *83*, 471.

(41) Wang, Y.; Loock, H.-P.; Cao, J.; Qian, C. X. W. *J. Chem. Phys.* **1995**, *102*, 808.